

Ultrathin conformal devices for precise and continuous thermal characterization of human skin

R. Chad Webb^{1†}, Andrew P. Bonifas^{1†}, Alex Behnaz², Yihui Zhang^{3,4}, Ki Jun Yu⁵, Huanyu Cheng⁴, Mingxing Shi⁶, Zuguang Bian^{4,7}, Zhuangjian Liu⁸, Yun-Soung Kim¹, Woon-Hong Yeo¹, Jae Suk Park⁵, Jizhou Song⁹, Yuhang Li⁴, Yonggang Huang⁴, Alexander M. Gorbach² and John A. Rogers^{1*}

Precision thermometry of the skin can, together with other measurements, provide clinically relevant information about cardiovascular health, cognitive state, malignancy and many other important aspects of human physiology. Here, we introduce an ultrathin, compliant skin-like sensor/actuator technology that can plially laminate onto the epidermis to provide continuous, accurate thermal characterizations that are unavailable with other methods. Examples include non-invasive spatial mapping of skin temperature with millikelvin precision, and simultaneous quantitative assessment of tissue thermal conductivity. Such devices can also be implemented in ways that reveal the time-dynamic influence of blood flow and perfusion on these properties. Experimental and theoretical studies establish the underlying principles of operation, and define engineering guidelines for device design. Evaluation of subtle variations in skin temperature associated with mental activity, physical stimulation and vasoconstriction/dilation along with accurate determination of skin hydration through measurements of thermal conductivity represent some important operational examples.

Traditional methods for skin thermography use either sophisticated infrared digital cameras for spatial imaging or simple, paste-on temperature sensors for single-point measurements. These and other related technologies have value in certain contexts, but they do not offer continuous, cost-effective precision mapping capabilities that are required for use at the point of care. For example, infrared cameras provide millikelvin precision and fine resolution in imaging, but they are expensive and require immobilization of the patient. Point contact sensors avoid these limitations, but they do not have the ability to perform spatial mapping, as typically required to extract meaningful information across the structurally and functionally heterogeneous surface of the skin. Such devices also irritate the skin and modify its natural physiological responses by thermally and mechanically loading its surface.

Here we introduce a class of thermal characterization technology that combines precision measurement with mapping capabilities, in a form that integrates intimately and non-invasively onto the surface of the skin. The devices incorporate microscale temperature sensors that can simultaneously act as micro-heaters (actuators), in arrayed layouts on thin, low modulus elastic sheets. The sensors/actuators rely on either thin serpentine features of thin metal (50 nm thick; Au) or PIN diodes constructed with nanoscale membranes of silicon (320 nm thick; Si nanomembranes). Integrated

collections of such components offer mechanical properties and geometries matched to human tissue¹, through advanced application of emerging concepts in stretchable electronics². A key enabling characteristic for use on the skin is the ability to provide soft, conformal contact with the epidermis in a manner that does not constrain or alter natural motions or behaviours. This epidermal² design enables robust adhesion with minimal irritation or discomfort, and without measurement artefacts that can arise from relative motion of the sensors/actuators and the skin or from interference with processes such as transdermal water loss. Here, we describe these technologies and illustrate their capabilities in continuous thermal characterization of the epidermis. Examples range from temperature measurement with a precision that matches the most sophisticated infrared cameras, to assessment of thermal conductivity and effects of blood flow on thermal transport.

We built two types of system. The first consists of arrays of temperature sensors that rely on the temperature coefficient of resistance (TCR) in thin (50 nm), narrow (20 μm) serpentine traces of gold, fabricated using microlithographic techniques (Supplementary Note S1) and configured for direct external addressing. The second exploits multiplexed arrays of sensors based on PIN diodes formed by patterned doping of Si nanomembranes (Supplementary Note S2). Here, changes in temperature cause well-defined shifts in the turn-on voltage. In both cases, the

¹Department of Materials Science and Engineering, University of Illinois at Urbana-Champaign, Urbana, Illinois 61801, USA, ²National Institute of Biomedical Imaging and Bioengineering, National Institutes of Health, Bethesda, Maryland 20892, USA, ³Center for Mechanics and Materials, Tsinghua University, Beijing 100084, China, ⁴Department of Civil and Environmental Engineering, Department of Mechanical Engineering, Center for Engineering and Health, and Skin Disease Research Center, Northwestern University, Evanston, Illinois 60208, USA, ⁵Department of Electrical and Computer Engineering, University of Illinois at Urbana-Champaign, Urbana, Illinois 61801, USA, ⁶School of Mechanics and Engineering, Southwest Jiaotong University, Chengdu 610031, China, ⁷Ningbo Institute of Technology, Zhejiang University, Ningbo 315100, China, ⁸Institute of High Performance Computing, 1 Fusionopolis Way, #16-16 Connexis, Singapore 138632, Singapore, ⁹Department of Mechanical and Aerospace Engineering, University of Miami, Coral Gables, Florida 33146, USA. †These authors contributed equally to this work. *e-mail: jrogers@illinois.edu

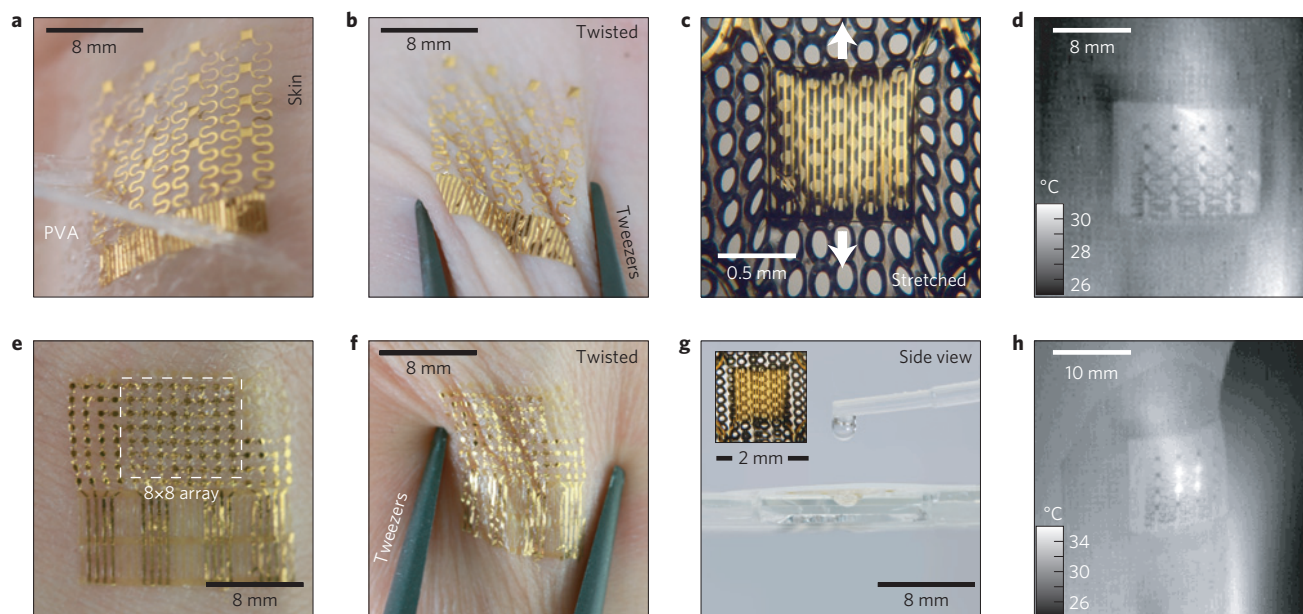


Figure 1 | Ultrathin, compliant, skin-like arrays of precision temperature sensors and heaters. **a**, Image of a 4×4 TCR sensor array after application to the skin using a water-soluble adhesive tape based on poly(vinyl alcohol). **b**, Similar device, deformed by pinching the skin in a twisting motion. **c**, Magnified image of a related device on a microperforated elastomeric substrate, under tensile strain. **d**, Infrared image of a 4×4 TCR sensor array mounted on the wrist at a location near the ulnar artery. **e**, Image of a 8×8 Si nanomembrane diode sensor array mounted on the skin. **f**, Similar device as deformed by pinching the skin in a twisting motion. **g**, Image of a 4×4 TCR sensor array mounted on microperforated elastomeric substrate, showing the ability of water to pass through readily. Inset: magnified image of a single TCR sensor on a microperforated substrate. **h**, Infrared image of a 4×4 TCR array on the human wrist while heating the four inner-most elements.

devices can be used as temperature sensors, as local microscale heaters, or as both, simultaneously. Figure 1 shows representative systems supported by thin ($50 \mu\text{m}$) uniform or microperforated elastomeric substrates, or integrated directly onto the human skin. The TCR device combines 16 sensors (each $\sim 1 \text{ mm} \times 1 \text{ mm}$, in a 4×4 layout) with interconnect traces ($30 \mu\text{m}$ wide and 600 nm thick) in a filamentary serpentine mesh. Thin layers of polyimide ($1.2 \mu\text{m}$) encapsulate these structures from above and below, to provide electrical insulation and a moisture barrier (Fig. 2a). This construction also places the metal close to the neutral mechanical plane, for improved mechanical robustness. The filamentary mesh design minimizes strain in the sensors and interconnects during deformation. The PIN system (Fig. 2c) combines 64 sensors (each $\sim 100 \mu\text{m} \times 200 \mu\text{m}$, an 8×8 layout) in a similar mesh structure, but with an interconnect design that allows multiplexed addressing. The resulting layout reduces the number of external connections from 128 (direct addressing) to 16 (multiplexed addressing), and allows straightforward scaling to increased numbers of sensors. The devices mount directly onto the skin or onto thin, uniform or microperforated sheets of silicone elastomer ($50 \mu\text{m}$, 30 kPa). Conformal attachment to the skin in all cases occurs through the action of van der Waals forces alone. The effective moduli of the systems are comparable to or smaller than that of the epidermis thereby yielding a type of integration that is mechanically invisible to the user. Devices are typically applied to skin that is mostly hairless (glabrous) or shaved. Small amounts of hair can be accommodated, as shown in Supplementary Fig. S1. A thin, flexible, conductive cable (Elform, HST-9805-210) establishes connection to external control and data acquisition electronics. Typical measurements involve averaged outputs sampled at 2 or 0.5 Hz , to yield precision (one standard deviation) of $\sim 12 \text{ mK}$ ($n = 222$) or $\sim 8 \text{ mK}$ ($n = 55$), respectively, as evaluated in control experiments. Use on human skin in hospital settings increases noise slightly, resulting in a precision of $\sim 23 \text{ mK}$ sampled at 2 Hz ($n = 300$) or $\sim 14 \text{ mK}$ sampled at 0.5 Hz ($n = 75$; Supplementary

Figs S2d,e and S3). This performance compares favourably to that of sophisticated infrared cameras, such as the one used in this work ($3.0\text{--}5.0 \mu\text{m}$ wavelength, 640×512 pixels, 14 bits per pixel; Santa Barbara Focalplane Array, Lockheed Martin), which has a measured sensitivity of $\sim 24 \text{ mK}$ (2 Hz sampling rate, $n = 300$; Supplementary Fig. S2f). We detected no hysteresis, within uncertainties, in the response of the sensors (Supplementary Fig. S4). Details of the set-up, calibration procedure and addressing schemes are given in Supplementary Note S3. Shown mounted on a human wrist in Fig. 2b, the epidermal sensor arrays reveal a spatial map of temperature (right) that matches well with the image obtained by the infrared camera (left). The scalability of the procedures for microfabrication provides straightforward routes to improved spatial resolution. The numbers of independently addressable sensors can be increased with multiplexing schemes that use the PIN diodes as switching elements. Figure 2d shows a temperature map (right) of a thin film copper heater, obtained with a PIN system (left).

The extremely thin and compliant construction of these devices provides important benefits. The first relates to mechanics. Here, the skin-like properties facilitate robust bonding to the skin without irritation, and enable effective isolation of the sensors/actuators from applied strain. This latter aspect is important because strain can change both the resistances and the turn-on voltages of the TCR and PIN sensors, respectively, in ways that could frustrate interpretation of the measurements. The open mesh, serpentine layouts, the neutral mechanical plane construction and the ultrathin device dimensions act together to minimize local strains on the sensors/actuators, even under relatively large system-level deformations. Motions of human skin involve a combination of wrinkling and stretching, to enable overall deformations of up to 100% in areas such as knees and elbows. The skin itself has a linear response to tensile strain up to $\sim 15\%$, nonlinear to $\sim 30\%$, and rupture at $>30\%$ (ref. 3), depending on factors including age and sun exposure⁴. Strain induced by wrinkling

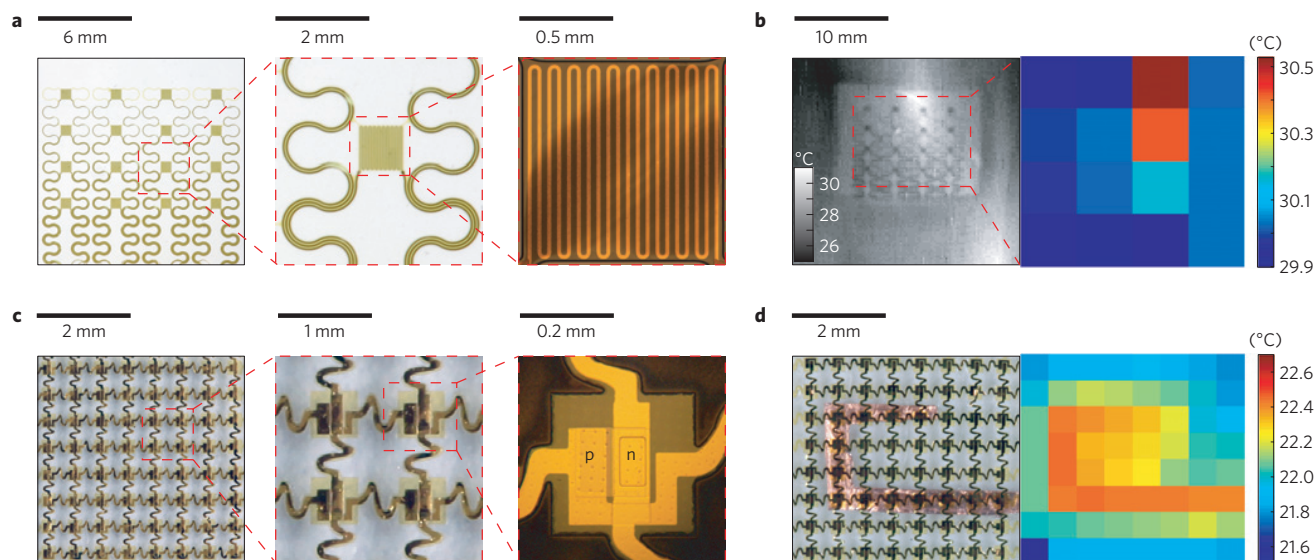


Figure 2 | Functional demonstrations of epidermal temperature sensors and heaters. **a**, Optical images of a 4×4 TCR sensor array integrated on a thin elastomeric substrate with magnified views of a single sensor. **b**, Infrared image of a similar device mounted on the skin of the human wrist (left) and map of temperature (right), where each pixel represents the reading of one sensor in the array. **c**, Optical images of a 8×8 Si nanomembrane diode sensor array integrated on a thin elastomeric substrate with magnified views of a single sensor. **d**, Optical image of a similar device mounted on a heated Cu element (left) and measured distribution of temperature (right).

can be well accommodated by the thin, neutral mechanical plane device designs. Tensile strains are relieved through microscale buckling and twisting of interconnect lines within the open mesh, serpentine layouts. Finite-element analysis (FEA) and experimental results (Supplementary Fig. S5) show, for example, that for a TCR device under a uniaxial strain of 10%, the average strains developed at the sensors/actuators are $<0.02\%$, corresponding to <50 mK shift in the apparent temperature (Supplementary Note S4). Similar FEA on PIN systems (Supplementary Note S4) indicates maximum principal strains $<0.55\%$ (Supplementary Fig. S6). In many practical cases, modest changes associated with these small strains can be eliminated with signal processing that exploits differences between characteristic frequencies associated with motion and changes in temperature.

The second consideration relates to thermal loading and response times, where the extremely low thermal masses (Supplementary Note S5) of the devices and their high degrees of water/gas permeability (Supplementary Note S6) are advantageous. For the case of devices laminated directly onto the skin with no elastomeric backing (Fig. 1a), the calculated thermal mass per unit area is $150 \mu\text{J cm}^{-2} \text{K}^{-1}$, which is the equivalent thermal mass per unit area of a layer of skin with thickness <500 nm, depending on hydration level. The addition of an elastomeric backing layer with thickness $\sim 50 \mu\text{m}$, which provides support for repeated application and removal of devices, raises the thermal mass per unit area to $7.2 \text{ mJ cm}^{-2} \text{K}^{-1}$, which is equal to $<25 \mu\text{m}$ of skin. Furthermore, the thermal inertia, a measure of the resistance of a system to changes in temperature, of the elastomer system is $\sim 500 \text{ W s}^{1/2} \text{ m}^{-2} \text{ K}^{-1}$, which is smaller than the value, $1,000\text{--}2,000 \text{ W s}^{1/2} \text{ m}^{-2} \text{ K}^{-1}$, for the skin itself^{5,6}. As a result, the sensor system can respond rapidly to changes in skin temperature. Test experiments (Supplementary Fig. S7) involving application of a heated droplet of glycol on a sensor reveal response times (~ 5 ms) that are far faster than any known physiological thermal process measurable at the surface of the skin. Analytical models quantitatively reproduce these time dynamics (Supplementary Note S7), thereby providing guidelines for optimized designs. For example, the polyimide encapsulation layers play key roles: increasing the thickness from 3.6 to $6.0 \mu\text{m}$ increases the response time from

3.7 to 13.1 ms. The combined effects of this small thermal mass and the permeability of the thin silicone substrates minimize physiological impacts. Temperatures measured with the infrared camera on the palm near a sensor device and directly underneath it (Supplementary Fig. S8a,b) show minimal differences. The effect of the system on skin hydration (Supplementary Fig. S8c) is also small, corresponding to an increase in relative skin hydration of $<6\%$ after 3 h of continuous use, as measured by a commercial moisture metre (Delfin MoistureMeterSC). Experiments conducted under conditions of profuse sweating demonstrate a situation that requires devices with no elastomeric backing to avoid disrupting natural processes. Devices with no elastomeric backing show no significant effect on skin temperature during profuse sweating, whereas devices with an elastomeric backing result in small temperature increases, $<2^\circ\text{C}$, directly beneath the device following high-intensity exercise (Supplementary Fig. S9).

Figure 3 summarizes results of measurements with a TCR device on the palm during applications of mental and physical stimuli. An immobilized configuration enables comparison to measurements with infrared images collected directly through the transparent regions of the device and in adjacent areas. The mental stimulus experiments involved 30 min of rest, followed by a series of mental math problems involving simple operators such as subtraction and division. Measurements of temperature from a representative sensor in the array and the results of spatially averaging data from a neighbouring region in the infrared image are shown in Fig. 3b. In the period before the mental stimulus, the data show clear temperature fluctuations of $0.1\text{--}1.0^\circ\text{C}$ at frequencies of $0.005\text{--}0.05$ Hz. Previous studies have indicated that skin on the palm has fluctuations in blood perfusion in this frequency regime due to the sympathetic activity of arteriovenous anastomoses^{7–10}. The remarkable level of agreement between the various measurements throughout this experiment establishes the precision and the absence of any effects of the device on natural thermal processes. Physical stimulus, involving gently rubbing together two fingers on the hand opposite to the one with the sensor, leads to qualitatively similar behaviours, with similar levels of agreement (Supplementary Fig. S3c).

The low-frequency oscillations evident in the data of Fig. 3d have diagnostic value for conditions such as congestive heart

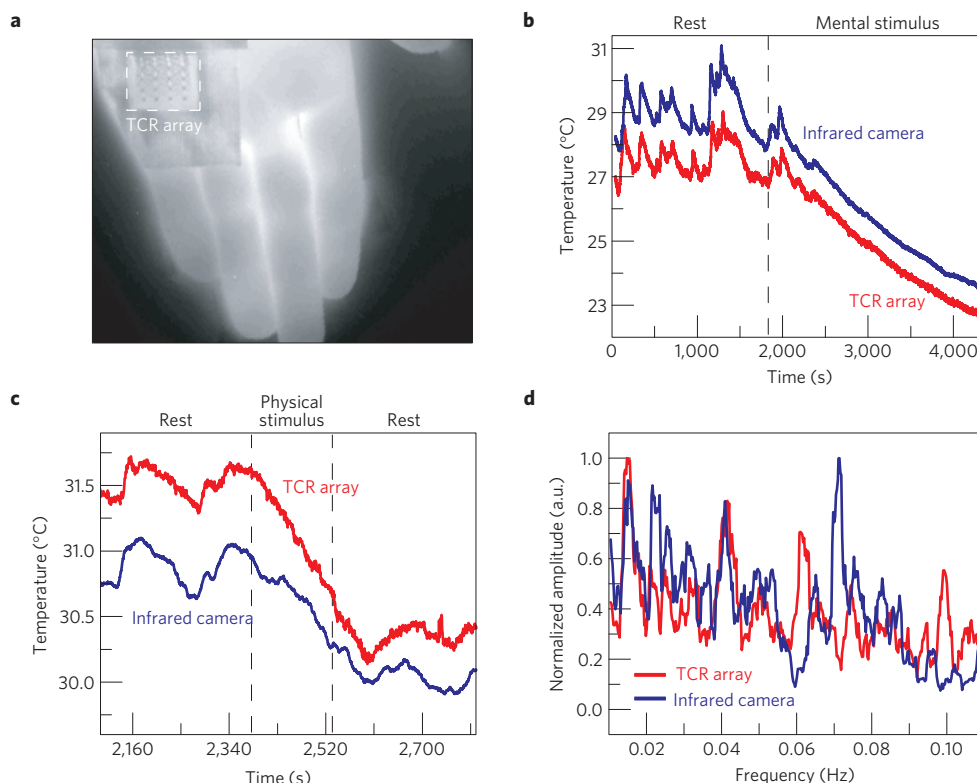


Figure 3 | Epidermal electronic evaluations of skin temperature at rest and during mental and physical stimulation. **a**, Infrared image of a 4×4 TCR sensor array mounted on the palm during stimulus experiments. **b,c**, Temperature of the palm measured with an infrared camera (blue) and a sensor array (red, offset for clarity) during mental (**b**) and physical stimulus tests (**c**). **d**, Normalized Fourier transform of temperature measured on the forearm using a TCR sensor array (red), and using infrared camera evaluation through a transparent region of the array (blue). Both measurements show prominent peaks around 0.01 and 0.04 Hz.

disease and tissue hypoxia¹¹, and disturbances in skin blood flow may reflect functional changes due to disease in other important organ systems¹². As small skin temperature changes correlate with tissue blood flow¹³, they can serve as naturally occurring markers for monitoring periodic contraction and dilation of the vessels (vasomotion). Previous studies of oscillatory behaviour in blood flow at low frequencies suggest correlations to local vasomotions controlled by endothelium-derived hyperpolarizing factor (0.005–0.0095 Hz), rate of endothelial release of nitric oxide (0.0095–0.02 Hz), and sympathetic activity (0.02–0.06 Hz; ref. 14.) Continuous temperature measurements on the forearm during a 60 min rest period demonstrate capabilities in this context (Fig. 3d). Here, the low-frequency power spectra of temperatures from a TCR device and the infrared camera exhibit peaks at ~ 0.01 Hz and ~ 0.04 Hz, probably corresponding to the types of vasomotion described above. Further information and results of control experiments are given in Supplementary Fig. S8d and Note S8.

In addition to use as passive monitors of natural processes, these sensors can measure time-dynamic changes associated with externally stimulated events. Figure 4 illustrates a cardiovascular screening procedure^{15,16} as an example of vasoconstrictive and vasodilative reactivity, where the vasculature adjusts blood flow through changes in vessel diameter in response to physiological stimuli¹⁷. Here, the device measures the temperature above the ulnar artery as part of a reactive hyperaemia protocol in which blood flow of the entire upper extremity is temporally occluded by a pressure cuff on the upper arm, and then the pressure is released. During the occlusion, the temperature of the skin (right above the ulnar artery) decreases markedly owing to lack of incoming blood flow and loss of heat to the environment. After the release of the occlusion, an overshoot in temperature

above the baseline level may occur because of an increase in blood flow above the initial value. Studies have shown that the extent of vasodilation¹⁸, maximal percentage increase in blood flow rate after occlusion¹⁶, and duration of reactive hyperaemia¹⁵ are valuable early indicators of the presence of cardiovascular risk factors. For example, the duration of reactive hyperaemia (defined as the time period between the release of occlusion and the return of blood flow to within 5% of the baseline value) was shown to be significantly lower in patients with hypercholesterolemia, diabetes mellitus, or in those who were smokers, as compared with healthy controls (80–95 s for those positive for risk factors as compared with 105–120 s for healthy controls)¹⁵, and the incidence of death due to cardiovascular events was shown to be significantly less likely in patients with a maximal blood flow rate $>105 \text{ cm s}^{-1}$ in the brachial artery during reactive hyperaemia as opposed to patients with smaller increases¹⁶. The responses of sensors across the array vary widely (Fig. 4c) owing to the localized thermal effect of the hyperaemic response of the ulnar artery, confirmed by the infrared image (Fig. 4b). The use of the spatial mapping array allows for useful measurement of the reactive hyperaemia response without precise placement of a single element above the artery. A thermal model of the human wrist (Supplementary Note S9 and Fig. S10) that considers the various tissues surrounding the ulnar artery, and quantitatively characterizes the heat exchange between the blood flow and the surrounding tissues, enables conversion of the measured changes in temperature (Fig. 4d, top) into changes in blood flow rate (Fig. 4d, bottom). The temporal variation of flow during the experiment can be approximated with a piecewise, exponential-type function, corresponding to the stages of pre-occlusion, vascular occlusion, and reperfusion after cuff pressure release^{19,20}. The parameters characterizing this function

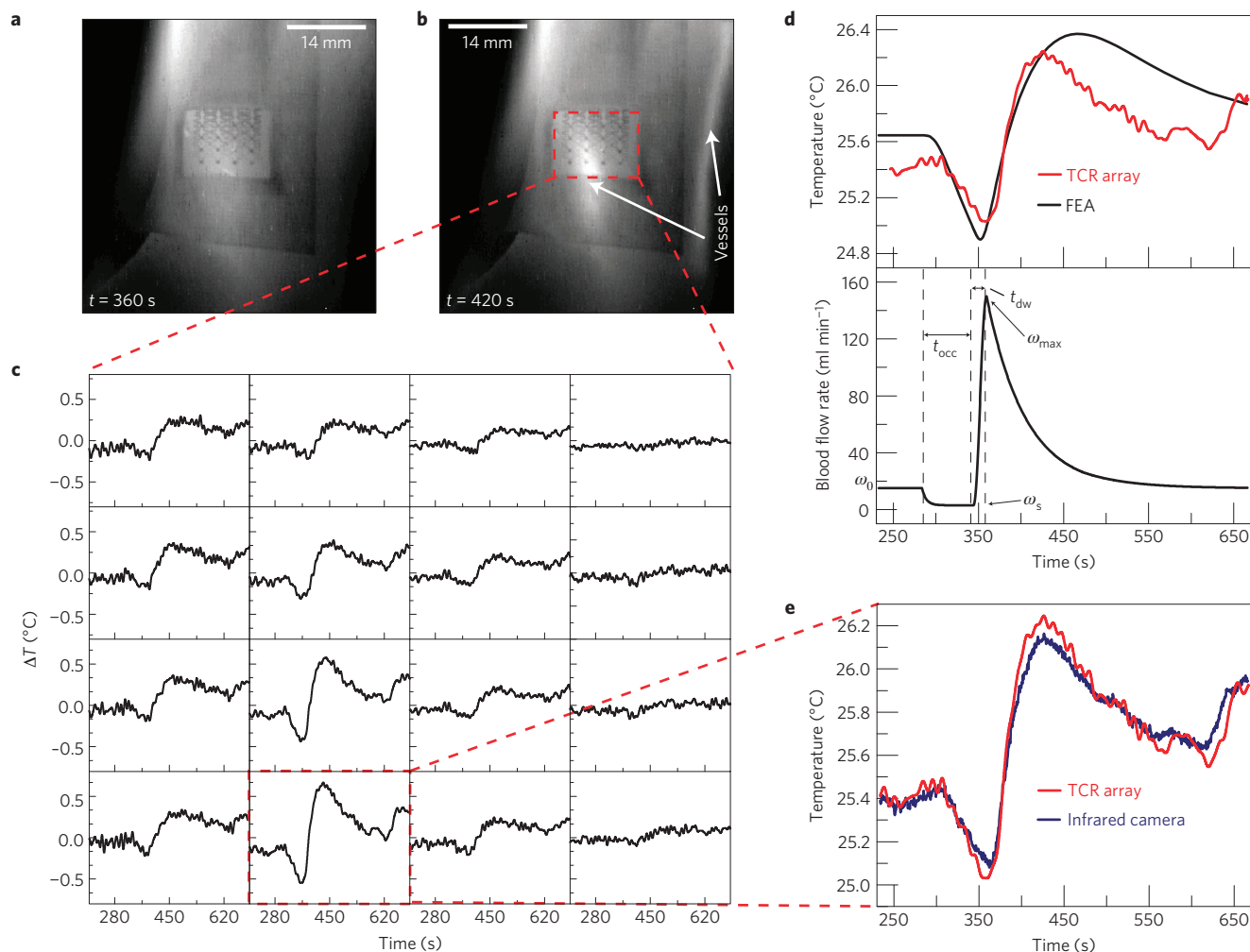


Figure 4 | Epidermal electronics for a reactive hyperaemia test. **a, b**, Infrared image of a 4×4 TCR sensor array on the wrist during an occlusion test at $t = 360$ s (corresponding to the end of a 60 s period of occlusion, during which there is minimal blood flow; **a**) and $t = 420$ s (corresponding to the peak in temperature rise after releasing the occlusion; **b**). **c**, Measured temperature changes during occlusion ($t = 300$ – 360 s) and after occlusion ($t = 360$ – 660 s) recorded by each of the 16 sensors in the 4×4 TCR sensor array. **d**, FEA of the temperature rise at the surface of the skin above the ulnar artery during the occlusion experiment as compared with experimental data (top) and blood flow rate through the ulnar artery used in the FEA (bottom). The key parameters characterizing the temporal variation of blood flow rate include: the occlusion time ($t_{\text{occ}} = 60$ s as used in the experiment; time-to-peak-flow ($t_{\text{dw}} = 15$ s; baseline flow rate ($\omega_0 = 15$ ml min $^{-1}$); occluded flow rate ($\omega_s = 3$ ml min $^{-1}$); peak flow rate ($\omega_{\text{max}} = 150$ ml min $^{-1}$). **e**, Temperature measured by the single sensor that showed the largest temperature change during the occlusion test.

are determined by the corresponding stages of temperature–time profiles derived from experimental measurement. Figure 4d demonstrates that the calculated temperature history using the thermal model can accurately account for the experimental results. For vessel diameters and depths that lie within reported ranges (Supplementary Note S9), the peak blood flow velocity after occlusion is calculated to be 98 cm s $^{-1}$, which represents a tenfold increase over the baseline of 9.8 cm s $^{-1}$, with a reactive hyperaemia duration of 127 s. These values match well with the literature^{15,16} for a person with low cardiovascular risk.

In comparison with conventional, point-contact sensors and infrared cameras, the technologies reported here offer an additional option for delivering precise levels of heating to the surface of the skin. An important example of the expanded capabilities that follow is a strategy for determining the local thermal conductivity. This parameter is of interest partly because it is known to serve as a useful proxy for free-water content⁵, as a simple methodology to monitor skin hydration and perspiration. In this mode, the temperature of a sensor element is measured during the application of constant current over two seconds, to create a small

temperature rise (<2 °C) on the skin. The thermal conductivity (k) of the skin is determined through a modification of the transient plane heat source method²¹ and standardized ISO-22007-2-2008 procedure, as outlined in Supplementary Note S10. Calibration can be performed with deionized water and ethylene glycol, and verified in four water/glycol mixtures (Fig. 5a). Figure 5c shows the temperature rise of a sensor element in contact with deionized water, air and the human forearm during measurement. A minimal power level of 1 mW, applied for two seconds, is required to obtain accurate measurements, as indicated by the large error bars associated with measurements with powers <1 mW in Fig. 5d. The characteristic depth of measurement, discussed in Supplementary Note S10, is approximately 500 μm . The simple correlation between the maximum rise in temperature and the reported thermal conductivity, shown as a shaded region in Fig. 5c and quantitatively in Fig. 5e, additionally provides a means to verify adequate sensor–skin thermal contact during long-term clinical monitoring. Figure 5e indicates excellent correspondence between thermal conductivity and hydration determined with a moisture meter (Delfin MoistureMeterSC) that uses electrical impedance.

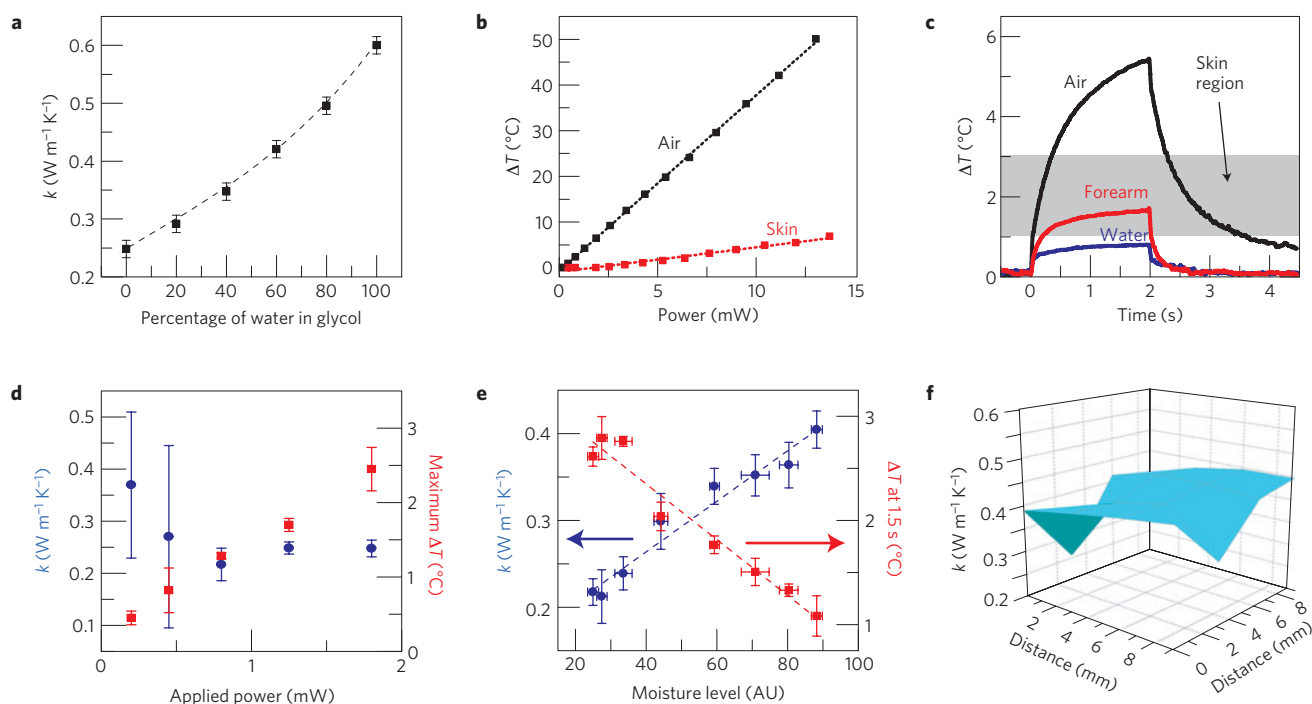


Figure 5 | Epidermal electronics configured for evaluating skin hydration and thermal conductivity. **a**, Thermal conductivity of water/ethylene glycol solutions as measured by a TCR heater/temperature sensor (points) and reported in the literature (dotted line). Error bars represent average standard deviations of six different ethylene glycol/water solution data sets, ten measurements each. **b**, Temperature rise as a function of Joule heating rate provided by a TCR heater/temperature sensor on an elastomeric backing, laminated onto the skin (red) and free-standing in air (black). **c**, Representative temperature rise during a 2 s period of heating on the elastomeric backing free-standing in air, laminated onto the human forearm, and with a drop of water on top. When laminated on skin, the temperature rise typically falls within the shaded region. **d**, Measured thermal conductivity (blue) and maximal temperature rise of the heater (red) as a function of Joule heating rate provided by a TCR heater/temperature sensor from $t = 0$ –2 s. Error bars represent standard deviations over ten measurements. The results indicate that a power of only ~ 1 mW enables reasonable signal to noise. **e**, Thermal conductivity (blue) and temperature rise at $t = 1.5$ s (red) as a function of skin hydration as measured with a commercial moisture meter (Delfin). The points and dotted lines represent measured data and modelling, respectively. Error bars represent standard deviations over ten measurements. The applied power in this case was 1.8 mW. **f**, Spatial mapping of thermal conductivity on the forearm, measured using a 4×4 TCR heater/sensor array.

Figure 5f demonstrates the use of this technique to generate a spatial map of thermal conductivity of the skin, by individual control of the actuators. Advantages of thermal measurements of hydration compared with those based on capacitance or impedance include the ability to isolate the electronics from the skin and to measure both temperature and thermal conductivity with a single system.

The results presented here demonstrate that unusual combinations of materials and device components in stretchable electronic systems can, when implemented with advanced modelling and analysis techniques, enable versatile, precision capabilities in thermal characterization of the skin. Several key features of operation suggest potential for practical use outside hospital settings, to provide real-time, clinical quality data for continuous health/wellness assessment. The microfabrication techniques used for these devices and the multiplexed schemes for addressing the sensors/actuators in them both scale in ways that create opportunities for substantially increased spatial resolution, with potential for monitoring of blood perfusion or localized thermogenesis associated with inflammatory events in tissues, as well as vascular tone and reactivity within well-defined vasculature territories, including capillary beds. Ongoing efforts into wireless device implementation will allow application of the techniques presented here to long-term studies with continuous precision thermal monitoring. Adapted versions of this technology may also allow intraoperative application to surgically exposed organs, including observation of high-frequency changes in vascular flow (for example, influenced by cardiac and respiratory

rates). Furthermore, the use of combined temperature sensing and microheating arrays in clinical research may create principally new diagnostic and therapeutic approaches for medicine. Use of local heating to create skin temporal windows for localized drug delivery through targeted microvascular territory²², non-invasive glucose monitoring²³, or local nutrient delivery critical for rapid, infection-resistant wound healing²⁴ represent additional possibilities of interest.

Methods

Fabrication of TCR devices. The fabrication, detailed in Supplementary Note S1, began with spin-coating of a thin film of polyimide (~ 1.2 μm , Sigma Aldrich) on a sacrificial layer of poly(methylmethacrylate) (100 nm, MicroChem). Metal-evaporation (Cr/Au, 5 nm/50 nm), photolithography and wet-etching steps defined serpentine-shaped TCR sensors. Additional polyimide spin-coating, oxygen reactive ion etching and metal deposition for contacts and interconnects completed the array, which was then transferred to a thin silicone support and bonded to a thin, flexible cable for external connection.

Fabrication of PIN devices. The fabrication, detailed in Supplementary Note S2, began by defining n- and p-doped regions on a silicon on insulator (320 nm Si on buried oxide) wafer. The doped regions were then transfer printed onto a Si wafer coated with poly(methylmethacrylate) and polyimide. Metal-evaporation, photolithography, chemical vapour deposition and wet-etching steps defined metallization layers. Additional polyimide spin-coating, oxygen reactive ion etching and metal deposition for contacts and interconnects completed the array, which was then transferred to a thin silicone support and bonded to a thin, flexible cable for external connection.

Thermal oscillation test. A volunteer (male, 28 years old) reclined in a chair with his left forearm gently secured to the armrest using Velcro strips to reduce

movement. A TCR device was placed on the ventral side of the left forearm and brought into thermal contact with a puff of compressed air. The infrared camera was placed 41 cm from the subject's left forearm, focused on the TCR device. The lights were then turned off ($t = 0$) and the subject was instructed to relax for 60 min. At $t = 60$ min the period of data acquisition ended.

Mental stimulus test. A volunteer (male, 28 years old) reclined in a chair with his left forearm secured gently to the armrest using Velcro strips to reduce movement. A TCR device was placed on the ventral side of the left forearm and brought into thermal contact with a low-velocity puff of compressed air. The infrared camera was placed 41 cm from the subject's left forearm, focused on the TCR device. The lights were then turned off ($t = 0$) and the subject was instructed to relax for 30 min. At $t = 30$ min an alarm sounded, and the subject was given a further 10 min of relaxation. At $t = 40$ min the subject began a series of mental arithmetic lasting 30 min. At $t = 70$ min the period of data acquisition ended.

Physical stimulus test. A volunteer (male, 28 years old) reclined in a chair with his left forearm secured gently to the armrest using Velcro strips to reduce movement. A TCR device was placed on the palm of the left hand and brought into thermal contact with a puff of compressed air. The infrared camera was placed 41 cm from the subject's left palm, focused on the palm at the location of the TCR device. The lights were then turned off ($t = 0$) and the subject was instructed to relax for 30 min. At $t = 30$ min an alarm sounded, and the subject was given a further 10 min of relaxation. At $t = 40$ min the subject began to rub the fingers of his right hand together for a period of 2 min. At $t = 42$ min the subject ceased rubbing and attempted to relax for a further 20 min. At $t = 62$ min the period of data acquisition ended.

Reactive hyperaemia test. A volunteer (male, 28 years old) reclined in a chair with his left forearm secured gently to the arm rest using Velcro strips to reduce movement. A pressure cuff was secured around the subject's left bicep. A TCR device was placed on the skin of the left wrist, volar aspect, approximately above the ulnar artery and brought into thermal contact with a puff of compressed air. The infrared camera was placed 41 cm from the subject's left wrist, focused on the location of the TCR device. The lights were then turned off ($t = 0$) and the subject was instructed to relax for 5 min. At $t = 5$ min the pressure cuff was inflated to a pressure of 250 mm Hg for a period of 1 min. At $t = 6$ min the pressure in the cuff was released. The subject was instructed to relax for 24 min. At $t = 30$ min the period of data acquisition ended.

Thermal conductivity and hydration measurements. Thermal conductivity was determined by analysing the temperature rise data from sensor elements during a 2 s period of heating. Each measurement occurred in three stages of measuring the voltage drop during a period of constant current using a Gamry Instruments Reference 600 Potentiostat: application of 100 μ A for 2 s, switching to 1.5 mA for 2 s (heating), and switching to 100 μ A for 2 s. This measurement was performed ten times on a single sensor, and the temperature rise data were analysed according to the transient plane source method, as outlined in Supplementary Note S10.

Received 13 March 2013; accepted 8 August 2013; published online 15 September 2013; corrected after print 26 September 2013

References

1. Wang, S. D. *et al.* Mechanics of epidermal electronics. *J. Appl. Mech.-T. ASME* **79**, 031022 (2012).
2. Kim, D. H. *et al.* Epidermal electronics. *Science* **333**, 838–843 (2011).
3. Arumugam, V., Naresh, M. D. & Sanjeevi, R. Effect of strain rate on the fracture behaviour of skin. *J. Biosci.* **19**, 307–313 (1994).
4. Agache, P. G., Monneur, C., Leveque, J. L. & De Rigal, J. Mechanical properties and Young's modulus of human skin *in vivo*. *Arch. Dermatol. Res.* **269**, 221–232 (1980).
5. Cohen, M. L. Measurement of thermal-properties of human-skin—review. *J. Invest. Dermatol.* **69**, 333–338 (1977).
6. Hassan, M. & Togawa, T. Observation of skin thermal inertia distribution during reactive hyperaemia using a single-hood measurement system. *Physiol. Meas.* **22**, 187–200 (2001).
7. Thoresen, M. & Walloe, L. Skin blood-flow in humans as a function of environmental-temperature measured by ultrasound. *Acta Physiol. Scand.* **109**, 333–341 (1980).

8. Lossius, K., Eriksen, M. & Walloe, L. Fluctuations in blood-flow to acral skin in humans—connection with heart-rate and blood-pressure variability. *J. Physiol.* **460**, 641–655 (1993).
9. Crandall, C. G., Meyer, D. M., Davis, S. L. & Dellaria, S. M. Palmar skin blood flow and temperature responses throughout endoscopic sympathectomy. *Anesth. Anal.* **100**, 277–283 (2005).
10. Jansky, L. *et al.* Skin temperature changes in humans induced by local peripheral cooling. *J. Therm. Biol.* **28**, 429–437 (2003).
11. Bernjak, A., Clarkson, P. B., McClintock, P. V. & Stefanovska, A. Low-frequency blood flow oscillations in congestive heart failure and after beta1-blockade treatment. *Microvasc. Res.* **76**, 224–232 (2008).
12. Holowatz, L. A., Thompson-Torgerson, C. S. & Kenney, W. L. The human cutaneous circulation as a model of generalized microvascular function. *J. Appl. Physiol.* **105**, 370–372 (2008).
13. Gorbach, A. M. *et al.* Infrared imaging of nitric oxide-mediated blood flow in human sickle cell disease. *Microvasc. Res.* **84**, 262–269 (2012).
14. Kvandal, P. *et al.* Low-frequency oscillations of the laser Doppler perfusion signal in human skin. *Microvasc. Res.* **72**, 120–127 (2006).
15. Ishibashi, Y. *et al.* Short duration of reactive hyperemia in the forearm of subjects with multiple cardiovascular risk factors. *Circ. J.* **70**, 115–123 (2006).
16. Huang, A. L. *et al.* Predictive value of reactive hyperemia for cardiovascular events in patients with peripheral arterial disease undergoing vascular surgery. *Arterioscler. Thromb. Vasc.* **27**, 2113–2119 (2007).
17. Nordin, M. Sympathetic discharges in the human supraorbital nerve and their relation to sudomotor and vasomotor responses. *J. Physiol.* **423**, 241–255 (1990).
18. Celermajer, D. S. *et al.* Non-invasive detection of endothelial dysfunction in children and adults at risk of atherosclerosis. *Lancet* **340**, 1111–1115 (1992).
19. Akhtar, M. W., Kleis, S. J., Metcalfe, R. W. & Naghavi, M. Sensitivity of digital thermal monitoring parameters to reactive hyperemia. *J. Biomech. Eng.* **132**, 051005 (2010).
20. Deshpande, C. *Thermal Analysis of Vascular Reactivity*. MS thesis, Texas A&M Univ. (2007).
21. Gustafsson, S. E. Transient plane source techniques for thermal conductivity and thermal diffusivity measurements of solid materials. *Rev. Sci. Instrum.* **62**, 797–804 (1991).
22. Park, J. H., Lee, J. W., Kim, Y. C. & Prausnitz, M. R. The effect of heat on skin permeability. *Int. J. Pharm.* **359**, 94–103 (2008).
23. Paranjape, M. *et al.* A PDMS dermal patch for non-invasive transdermal glucose sensing. *Sens. Actuat. A* **104**, 195–204 (2003).
24. Ikeda, T. *et al.* Local radiant heating increases subcutaneous oxygen tension. *Am. J. Surg.* **175**, 33–37 (1998).

Acknowledgements

This material is based on work supported by the National Science Foundation under Grant No. DGE-1144245, Grant No. ECCS-0824129 and through the Materials Research Laboratory and Center for Microanalysis of Materials at the University of Illinois at Urbana-Champaign. J.A.R. acknowledges financial support through a National Security Science and Engineering Faculty Fellowship. The work on silicon nanomembranes was financially supported by a MURI grant from the Air Force Office of Scientific Research. This research was supported in part by the Intramural Research Program of NIBIB, NIH. The authors would like to thank H. Eden for his invaluable critique and insightful comments during preparation of this manuscript.

Author contributions

A.P.B., R.C.W., A.B., A.M.G. and J.A.R. designed the experiments. A.P.B., R.C.W., K.J.Y., Y.-S.K., W.-H.Y. and J.S.P. carried out the fabrication. A.P.B., R.C.W., A.B., A.M.G. and J.A.R. carried out experimental validation and data analysis. Y.Z., Z.B., J.S., Y.L. and Y.H. contributed to the thermal modelling of sensor response time and reactive hyperaemia. H.C., M.S., Z.L. and Y.H. contributed to the mechanical modelling of strain. R.C.W., A.P.B., A.B., Y.Z., H.C., Z.B., Y.H., A.M.G. and J.A.R. co-wrote the paper.

Additional information

Supplementary information is available in the [online version of the paper](#). Reprints and permissions information is available online at www.nature.com/reprints. Correspondence and requests for materials should be addressed to J.A.R.

Competing financial interests

The authors declare no competing financial interests.

Ultrathin conformal devices for precise and continuous thermal characterization of human skin

R. Chad Webb, Andrew P. Bonifas, Alex Behnaz, Yihui Zhang, Ki Jun Yu, Huanyu Cheng, Mingxing Shi, Zuguang Bian, Zhuangjian Liu, Yun-Soung Kim, Woon-Hong Yeo, Jae Suk Park, Jizhou Song, Yuhang Li, Yonggang Huang, Alexander M. Gorbach and John A. Rogers

Nature Materials **12**, 938–944 (2013); published online 15 September 2013; corrected after print 26 September 2013.

In the version of this Article originally published, in Fig. 3b,c the labels at the top of the graphs were missing. This error has been corrected in the HTML and PDF versions of the Article.